nature geoscience

ARTICLES

https://doi.org/10.1038/s41561-018-0209-2

Forced subduction initiation recorded in the sole and crust of the Semail Ophiolite of Oman

Carl Guilmette[1*], Matthijs A. Smit[2], Douwe J. J. van Hinsbergen[3], Derya Gürer[3], Fernando Corfu[4], Benoit Charette[5], Marco Maffione[6], Olivier Rabeau[1] and Dany Savard[7]

Subduction zones are unique to Earth and fundamental in its evolution, yet we still know little about the causes and mechanisms of their initiation. Numerical models show that far-field forcing may cause subduction initiation at weak pre-existing structures, while inferences from modern subduction zones suggest initiation through spontaneous lithospheric gravitational collapse. For both endmembers, the timing of subduction inception corresponds with initial lower plate burial, whereas coeval or delayed extension in the upper plate are diagnostic of spontaneous or forced subduction initiation, respectively. In modern systems, the earliest extension-related upper plate rocks are found in forearcs, but lower plate rocks that recorded initial burial have been subducted and are inaccessible. Here, we investigate a fossil system, the archetypal Semail Ophiolite of Oman, which exposes both lower and upper plate relics of incipient subduction stages. We show with Lu–Hf and U–Pb geochronology of the lower and upper plate material that initial burial of the lower plate occurred before 104 million years ago, predating upper plate extension and the formation of Semail oceanic crust by at least 8 Myr. Such a time lag reveals far-field forced subduction initiation and provides unequivocal, direct evidence for a subduction initiation mechanism in the geological record.

The sinking of cold lithosphere in the Earth's mantle along subduction zones is widely recognized as the main driving force for global plate tectonics[1]. Despite decades of research, the processes and mechanisms of subduction initiation remain controversial[2]. Two main conceptual end-member mechanisms considered are 'induced' and 'spontaneous' subduction initiation[2,3] (Fig. 1). Induced subduction initiation (ISI) requires a period of forced convergence, presumably accommodated at a pre-existing favourably orientated weak structure, until subduction eventually becomes self-sustained[4–6]. Alternatively, gravitational instability across oceanic transform faults or passive continental margins has been proposed to trigger lithospheric collapse and spontaneous subduction initiation (SSI) without net plate convergence[3,7]. Whether only one of ISI or SSI is the active subduction initiation mode on Earth, or both modes can be activated depending on the tectonic setting, is a matter of debate[2,3]. A fundamental criterion that would discern between ISI and SSI is the time lag between initial lower plate burial and the ensuing upper plate extension (Fig. 1). During SSI, the area consumed by subduction must simultaneously be balanced by area gained through upper plate extension[7,8]. In contrast, upper plate extension following ISI must be generated by the growing slab after a period of forced underthrusting[4,5,9], resulting in a time lag of several millions of years. Constraining the magnitude of this time lag requires specific geochronological methods applied to a rock record of both the formation of the incipient subduction thrust and the onset of upper plate extension.

Models for subduction initiation are based on studies of earliest extension and magmatism in the forearc of modern subductions such as the Izu–Bonin–Marianna system[7,10], where rocks that directly recorded formation of the subduction interface are not exposed. Subduction initiation is widely assumed to have been spontaneous in this system[7,8,11]. Accordingly, the causes and consequences of subduction initiation are sought for in the tectonic setting at the time of forearc extension[12]. To date, the early subduction initiation history remains elusive[2], and ISI may have begun millions of years before forearc extension.

Research on supra-subduction zone (SSZ) ophiolites and associated metamorphic soles may yield more comprehensive insights into subduction initiation, because these provide a rock record of both upper plate extension and lower plate burial[2], respectively. SSZ ophiolites[13,14] are interpreted as relic forearc oceanic lithosphere—similar in composition to the Izu–Bonin–Marianna forearc—that formed during subduction initiation[7–9] and was subsequently uplifted above sea level[15]. Many SSZ ophiolites rest on thin (<500 m) sheets of metamorphosed oceanic crust termed metamorphic soles. These metamorphic soles derive from the uppermost crust of the subducting lower plate[16–19] that was preserved from further subduction by 'welding' to the mantle section of the upper plate during subduction zone infancy[20,21]. Garnet–clinopyroxene amphibolites found at the top of many metamorphic soles indicate high-pressure granulite facies[22,23] peak metamorphic conditions (11–13 kbar and 850 °C). Metamorphism of oceanic crust to such conditions requires subduction along an anomalously hot geothermal gradient that is restricted to the initiation stage of a subduction zone[20,21,24]. These amphibolites probably represent the leading edge of the nascent slab and may therefore have directly recorded the initial burial of the lower plate during nucleation of a subduction interface[18,20,21].

The age of extension and crustal accretion in ophiolites is commonly estimated using U–Pb dating of zircon from gabbros and plagiogranites, interpreted to have formed in magma chambers below a spreading ridge[25,26]. Dating of the earliest history of the subduction interface requires an estimation of the age of

[1]E4m, Département de Géologie et de Génie Géologique, Université Laval, Québec, Québec, Canada. [2]PCIGR, Department of Earth, Ocean and Atmospheric Sciences, University of British Columbia, Vancouver, British Columbia, Canada. [3]Department of Earth Sciences, Utrecht University, Utrecht, the Netherlands. [4]Department of Geosciences and CEED, University of Oslo, Oslo, Norway. [5]Department of Earth and Environmental Sciences, University of Waterloo, Waterloo, Ontario, Canada. [6]School of Geography, Earth and Environmental Sciences, University of Birmingham, Birmingham, United Kingdom. [7]LabMaTer, Département de Génie Géologique, Université du Québec à Chicoutimi, Chicoutimi, Québec, Canada. *e-mail: carl.guilmette@ggl.ulaval.ca

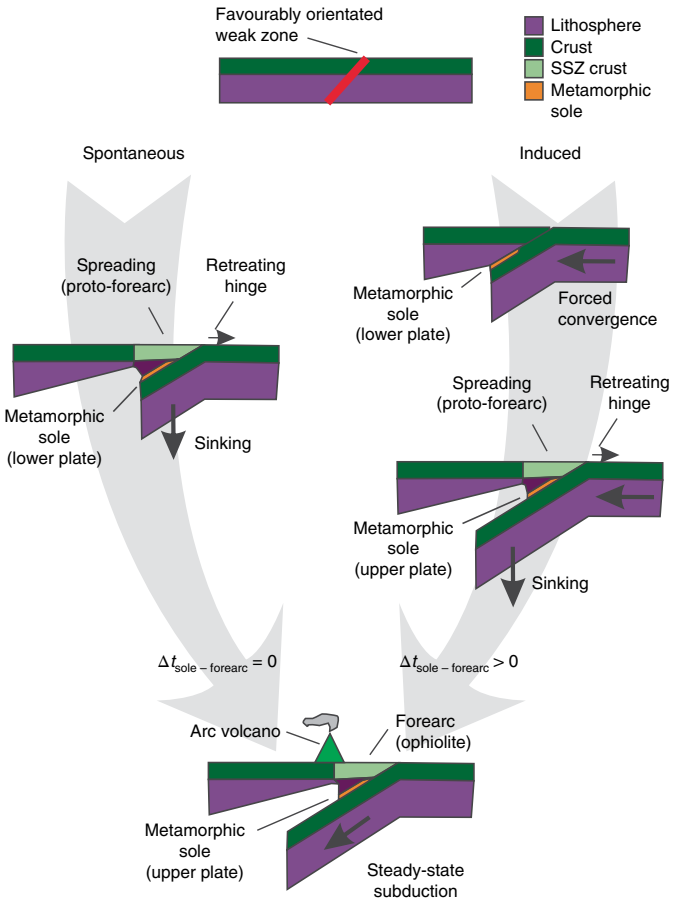

Fig. 1 | Conceptual lithospheric sections representing SSI versus ISI. The time lag between initial lower plate burial and incipient upper plate extension is diagnostic of the subduction initiation mode.

prograde metamorphism in the garnet–clinopyroxene amphibolites of metamorphic soles. Previous chronological studies of soles used $^{40}Ar/^{39}Ar$ hornblende or mica dating[9,18,20,27,28] and, more recently, U–Pb dating of zircons from melt segregations[29,30]. These ages typically coincide or slightly post-date the ages of the magmatic crust of the overlying ophiolite[9,18,28]. Coinciding $^{40}Ar/^{39}Ar$ and U–Pb dates from sole rocks, and age data for ophiolitic crustal spreading have been taken to provide evidence for synchronous sole formation and upper plate spreading[28,29]. The meaning of this coincidence in terms of sole formation is nevertheless debated[9]. Both methods date post-peak conditions rather than burial[31], and thus underestimate the age of sole formation by a yet-unknown amount of time.

It is clear that rigorously constraining the chronology of subduction initiation requires new approaches in dating the earliest metamorphic minerals in soles. A promising technique is Lu–Hf dating of garnet—a petrological indicator of burial and heating in metamorphosed oceanic rocks. Owing to the robustness of the chronometer at high temperatures (900–950 °C)[32–34], prograde age records of garnet growth are typically well preserved even in cases of long-lived supra-solidus conditions[35]. Here, we apply this approach to garnet from the metamorphic sole of the archetypal Semail Ophiolite of Oman to date the early stages of sole development. The results, supported by textural observations and trace element mineral chemistry, are then combined with new U–Pb zircon and titanite data, and existing dates for the sole and overlying ophiolitic crust, to investigate the complete history of the sole, from burial and heating to exhumation and cooling. The comparison of garnet growth ages in the metamorphic sole and published extension ages in the overlying ophiolite constrains a minimum time lag between initial subducting plate burial and incipient upper plate extension.

The Semail Ophiolite. The Semail Ophiolite (Fig. 2a) exposes over 20,000 km^2 of oceanic crust and upper mantle rocks underlain by a discontinuous thin sheet of metamorphic sole. The ophiolite–sole couple is thought to have been emplaced in Late Cretaceous time as a giant thrust sheet[36] over the Hawasina complex comprising distal oceanic rocks, and carbonates of the Arabian passive margin[37]. The Semail Ophiolite exposes a section of oceanic lithosphere including residual upper mantle rocks made of harzburgite and dunite, plutonic lower and middle crust comprising cumulates and gabbros, and an upper crustal sheeted dyke complex underlying pillowed to massive submarine basalts and abyssal sediments[38] (Fig. 2). High-precision U–Pb dating of the plutonic section across the ophiolite showed that the oceanic crust of the ophiolite was generated during rapid spreading between 96.1–95.5 million years ago (Ma)[25,26].

The ophiolite has been classically interpreted as a relic fast-spreading mid-ocean ridge[38,39]. However, recent evidence clearly shows that the ophiolite formed above an active subduction zone[29,40,41]. Similarities in the chemostratigraphy of the Semail Ophiolite and the Philippine Sea Plate forearc strengthened the inference that the ophiolite formed during subduction initiation[2,13] (either spontaneous[3,8,42] or induced[43,44]).

The sole of the Semail Ophiolite comprises amphibolites that are notably garnet- and clinopyroxene-bearing near the contact with mantle rocks. Garnet–clinopyroxene sole amphibolites represent oceanic upper crustal mid-ocean ridge basalt (MORB)-like basaltic sequences[40] of unknown age, which were metamorphosed to peak conditions of 11–13 kbar and 850 °C[21,45,46]. U–Pb dating of zircon from melt segregations suggests solidification of the melt fraction by 96.16–94.5 Ma[26,29,30], followed by rapid cooling below the closure temperature of the $^{40}Ar/^{39}Ar$ system in hornblende (500–550 °C) between 95.7 and 92.6 Ma[28]. The available data support the hypothesis that the upper crustal protolith of the sole was subducted to mantle depths in excess of 35 km along an incipient hot subduction plane before being transferred to the upper plate[20,21].

This study focuses on two main Omani metamorphic sole localities: Wadi Tayin and Wadi Sumeini (Fig. 2). The Wadi Tayin locality[21,45] (Fig. 2b) exposes amphibolites interlayered with thin quartz- and calc-silicate-rich layers, overlain by a middle quartzite-dominated interval, and again an amphibolite layer with garnet- and clinopyroxene-bearing amphibolites present in the top 5 m (Fig. 2e). The Sumeini sole locality[45,46] (Fig. 2c) also exposes amphibolites, which become garnet- and clinopyroxene-bearing in the upper 10 m (Fig. 2d), whereas the lower section of the sole consists of epidote amphibolite with more abundant quartzite and marble. We collected samples WT-150 and WT-151 from the Wadi Tayin locality and SU-03A from the Sumeini sole locality (Fig. 2b–e) from garnet- and clinopyroxene-bearing amphibolites that occur as metre-scale coherent levels (Fig. 2d) or as boudins embedded in garnet-free amphibolite (Fig. 2e) immediately below the contact with the overlying mantle section.

Occurrence, composition and age of garnet, zircon and titanite. The samples show a hornblende-dominated nematoblastic fabric that wraps around boudinaged bands of garnet–clinopyroxene-rich granulite (Fig. 3a–c). Garnet occurs as subhedral centimetre-scale porphyroblasts with abundant inclusions (Fig. 3). Mineral compositions are consistent with those of similar samples used in previous petrological studies[21,45,46] and with high-pressure granulite facies metamorphic conditions[22,23]. The strongly foliated matrix is defined by subhedral hornblende and subordinate anhedral diopside with abundant pseudomorphed anhedral plagioclase and fine-grained ilmenite–titanite symplectites. The granulite assemblage is variably overprinted by dynamic amphibolite–facies metamorphism. Sample

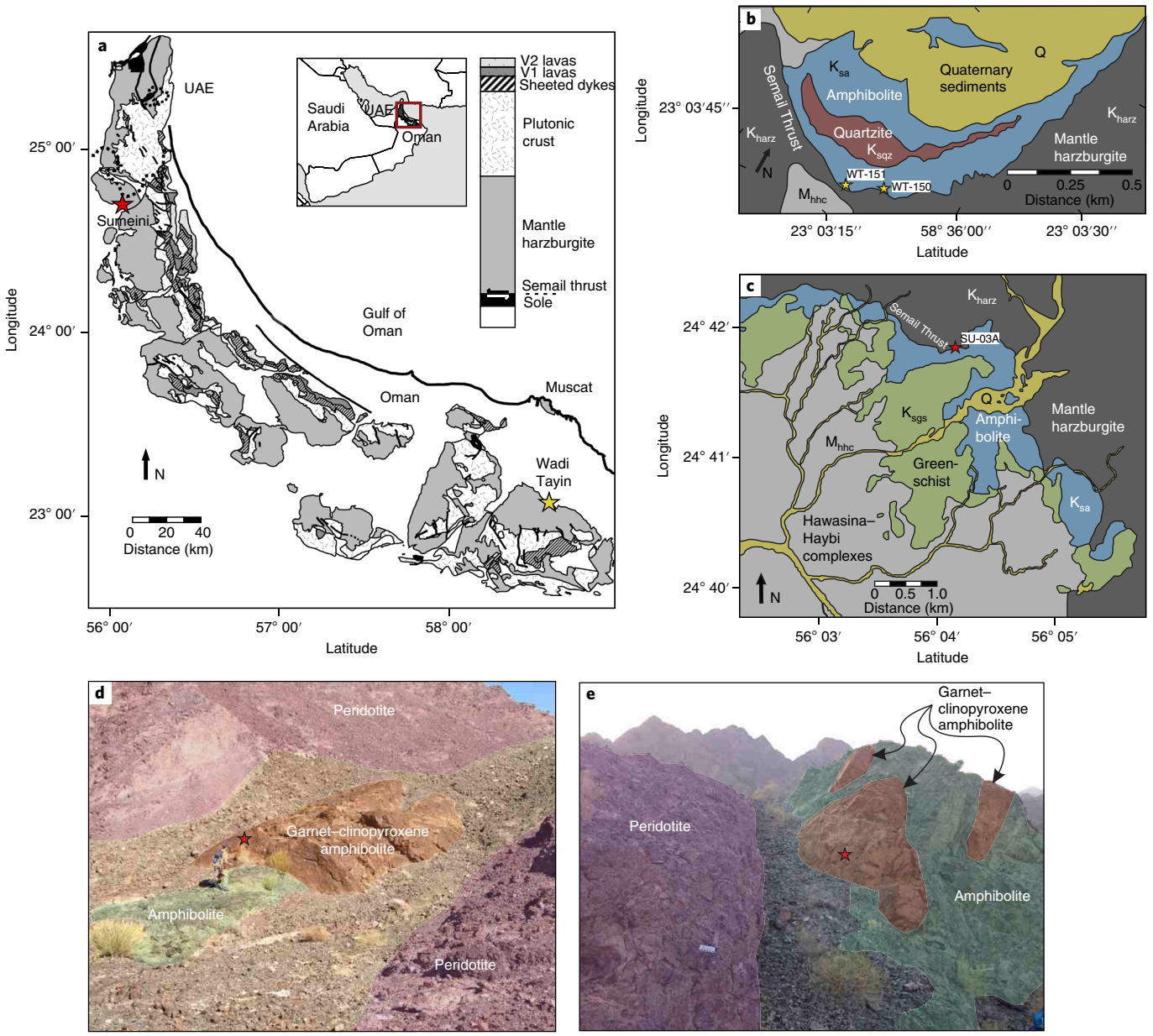

Fig. 2 | Geological maps, sample locations and field relationships. a, Geological map of Oman. **b**,**c**, Geological maps and sample locations at Wadi Tayin (**b**) and Sumeini (**c**). **d**,**e**, Field relationships for samples SU-03 (**d**) and WT-151 (**e**). Scale bar on the peridotite outcrop of **e**, 10 cm. Panels **a**–**c** adapted from ref. [29], Elsevier. Red stars are sampling sites. K_{harz}, Cretaceous harzburgite; K_{sqz}, Cretaceous sole – quartzite; K_{sa}, Cretaceous sole – amphibolite; K_{sgs}, Cretaceous sole – greenschist; Q, Quaternary; M_{hhc}, Hawasina and Haybi complexes.

SU-03A best preserves the granulite assemblage, whereas sample WT-150 shows the strongest amphibolite overprint. A lower-grade assemblage with epidote, prehnite and albite is found in fractures and veins, and as pseudomorphic replacements of plagioclase; the mafic minerals of the granulite assemblages are not substantially affected by such replacement.

Garnet shows complex zoning and inclusion patterns that differ between samples. Two garnet zones (grt-1 and grt-2) are nevertheless consistently observed. Grt-1 is defined by anhedral cores that are generally richer in calcium, manganese and heavy rare earth elements (HREE) (Figs. 3 and 4). These cores are typically poikiloblastic with inclusions of titanite and apatite in the innermost domains (grt-1a) and mono- and polymineralic inclusions of diopside, hornblende, plagioclase, ilmenite, titanite and apatite in the outer domains (grt-1b). Polymineralic inclusions locally show negative shapes and very low dihedral angles (Figs. 3f,g), suggesting that they represent the solidification product of trapped melt. Grt-1a shows distinctly lower chondrite-normalized gadolinium/ytterbium (Gd_N/Yb_N) than grt-1b. Grt-2 is defined by a textural and compositional mantle that encloses anhedral grt-1 cores. Grt-2 has fewer inclusions, is magnesium-rich and calcium-poor relative to grt-1, has high Gd_N/Yb_N, and shows strong and locally very well-defined oscillatory zoning for HREE (Fig. 4).

All three samples yielded garnet–whole rock Lu–Hf isochrons (Fig. 5a–c) with mean square weighted deviation (MSWD) between 0.32 and 0.79, and uncertainties of 0.8% relative standard deviation or better. The samples from Wadi Tayin yielded ages of 104.1 ± 1.1 Ma (MSWD = 0.79; sample 150A) and 103.2 ± 1.2 Ma (MSWD = 0.32; sample 151A), and sample SU-03A from Sumeini yielded an age of 103.5 ± 1.6 Ma (MSWD = 0.62). All Lu–Hf age data

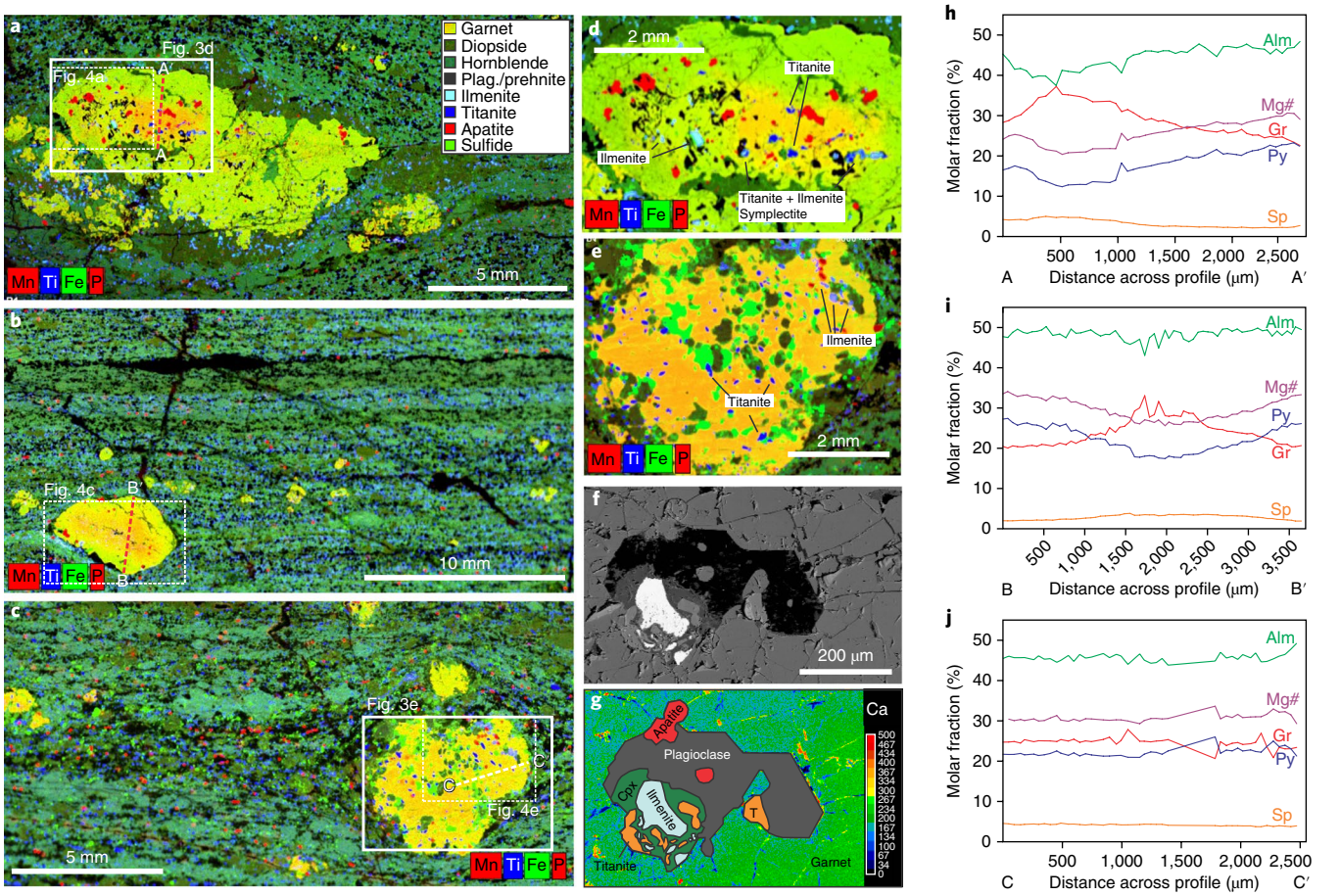

Fig. 3 | Petrography of the investigated samples. a–c, Micro-X-ray fluorescence chemical maps of thin sections for the samples SU-03A (**a**), WT-150 (**b**) and WT-151 (**c**). **d**, Magnified view of the solid boxed area in **a**. **e**, Magnified view of the solid boxed area in **c**. **f**,**g**, Back-scatter detector image (**f**) and composite Ca map + schematic (**g**) of a melt pseudomorph inclusion in garnet from SU-03A. The colour scale in garnet in **g** represents Ca relative abundance. **h–j**, Electron probe microanalyser chemical profiles for the samples SU-03A (**h**), WT-150 (**i**) and WT-151 (**j**), showing almandine (Alm), grossular (Gr), pyrope (Py) and spessartine (Sp) mole fractions and $Mg\# = Mg^{2+}/(Mg^{2+} + Fe^{2+})$. The locations of the A–A′, B–B′ and C–C′ profiles in **h–j** are indicated by dashed lines in **a–c**, respectively. Plag., plagioclase; Cpx, clinopyroxene.

are identical within uncertainty. Taking a weighted mean of these ages yielded 103.7 ± 0.7 Ma (MSWD = 0.63), indicating no resolvable age scatter among the samples.

Zircon and titanite grains were recovered from sample WT-151. The zircon population consists largely of colourless, subequant and anhedral grains (Fig. 5d). Five analyses of such grains are clustered to the right of the concordia curve. The slight discordance and spread in $^{207}Pb/^{235}U$ is a common feature of young zircon populations, reflecting in part the probable bias in the decay constants used and initial ^{231}Pa excess[47]. All five $^{206}Pb/^{238}U$ ages overlap within error, yielding a robust average age of 96.19 ± 0.14 Ma for the crystallization of zircon. A fraction of four titanite grains provides a $^{206}Pb/^{238}U$ age of 95.60 ± 0.27 Ma.

Garnet growth in the Omani Ophiolite soles. The microtextures and major and trace element distributions described above indicate the following growth history (Fig. 6). Grt-1 nucleated and initially grew at sub-solidus conditions in the titanite stability field. The transition from grt-1a to grt-1b marks the prograde stabilization of ilmenite and the formation of inclusions indicative of the first occurrence of melt. Peritectic garnet growth at those conditions is further supported by evidence of melt segregations at the outcrop scale[29,30] and by phase equilibria modelling[21,23]. The distinct increase in Gd_N/Yb_N could relate to the dehydration melting of hornblende or titanite breakdown. Grt-2 represents peritectic garnet, as indicated by its oscillatory zoning. This zoning is interpreted to reflect the competition between the rates of HREE uptake by growing garnet and diffusive HREE supply within the melt. Such a garnet growth sequence is consistent with phase equilibria modelling and experiments for MORB-like protoliths that predict supra-solidus grt-2 growth[21,23] from 9 kbar and 650 °C to 11 kbar and 850 °C across the titanite–ilmenite transition[48].

The robustness of the Lu–Hf geochronometer[33,34] is largely governed by the low diffusivity of hafnium[49]. The closure temperatures of diffusive hafnium loss for the grains analysed were at least 900 °C[33] and hence exceed peak temperatures that the Omani sole samples were subjected to. Lutetium is more mobile, and modelled mechanisms of age skewing by diffusive lutetium redistribution[49] must be considered. However, these are clearly not applicable here. The dated samples show exceptional preservation of the fine growth zoning in the distributions of lutetium, which precludes any significant diffusive homogenization of lutetium after garnet growth. The dates, which were determined for bulk-grain garnet populations, therefore represent an estimate of the average age of garnet growth weighted according to lutetium distribution. The Lu–Hf dates for all three samples are identical, yet show different lutetium distributions. This shows that the weighing of ages was insignificant. Our data are thus best explained by a single, fast garnet growth event at sub- to supra-solidus conditions from roughly 550 °C and 8 kbar to peak conditions of 850 °C and 11–13 kbar (Fig. 6). Zircon

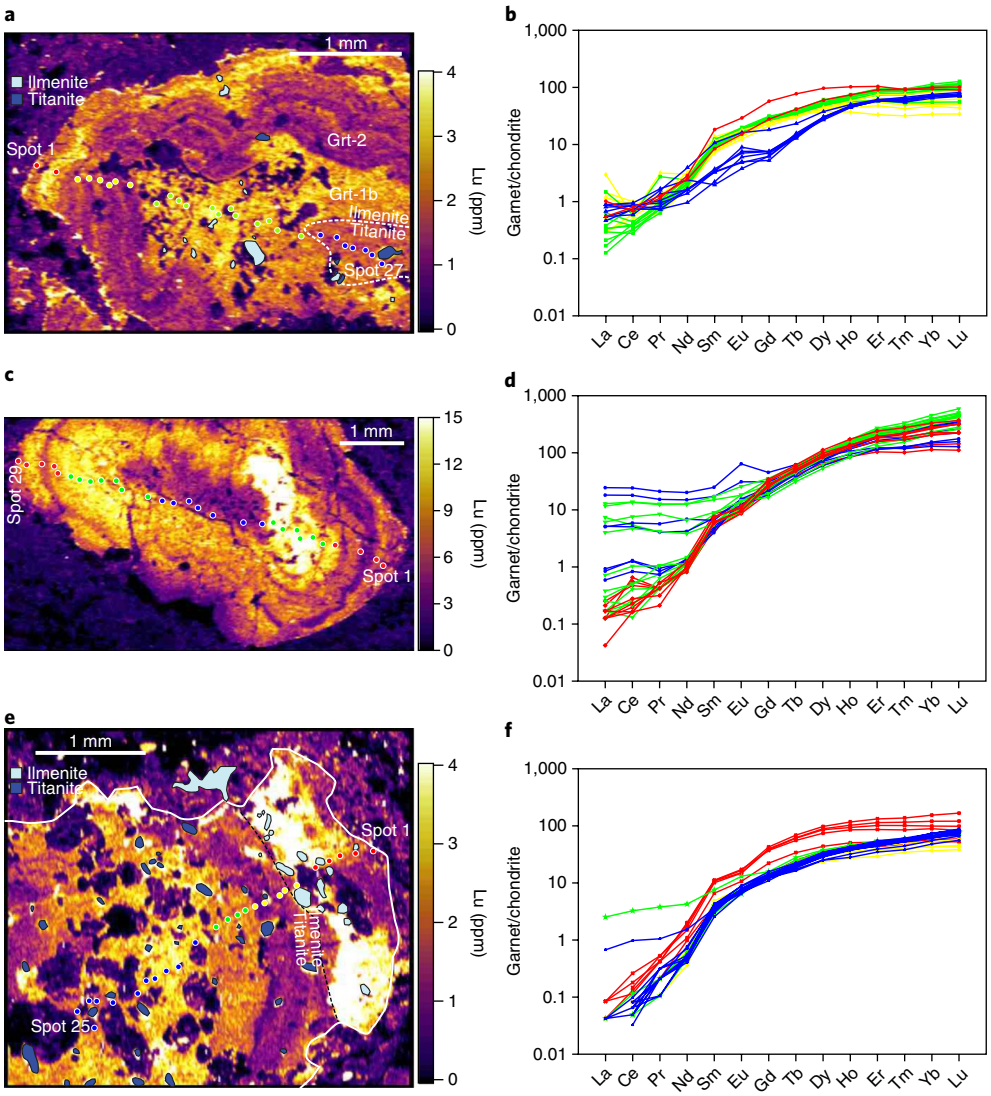

Fig. 4 | Trace element content of representative garnet from samples SU-03A, WT-150 and WT-151. a,**c**,**e**, Lutetium maps for SU-03A (**a**), WT-150 (**c**) and WT-151 (**e**), the locations of which are indicated by the dashed squares in Fig. 3a–c, respectively. **b**,**d**,**f**, Rare earth element (REE) profiles normalized to chondrites[51]. The locations of the spot analyses are shown **a**, **c** and **e**, respectively.

(96.19 ± 0.14 Ma) may have crystallized from late, highly fractionated solidifying trapped melt[29,31] when the rocks cooled from peak conditions to sub-solidus conditions of 700 °C. The U–Pb dates of titanite (95.60 ± 0.27 Ma) represent cooling below 650–600 °C[31].

Implications for subduction initiation. Rheological studies indicate that the upper part of a subducting oceanic plate will be transferred to the upper plate when conditions of 850 °C and 11–13 kbar are reached at the interface, forming a metamorphic sole[20,21]. We now show that garnet growth in the sole under the Semail Ophiolite occurred at 104 Ma. This age provides a timing for burial, decoupling from the lower plate and transfer to the upper plate. Between peritectic garnet growth at 104 Ma and zircon crystallization at 96 Ma, the welded sole did not record any major thermal or dynamic perturbation, probably staying at supra-solidus peak conditions while underthrusting progressed. Around 96 Ma, extension in the upper plate led to oceanic lithosphere accretion along a spreading centre. From 96.2–94.5 Ma, zircon crystallized from the segregated melt fractions[29,30] in the underlying metamorphic sole, marking cooling to sub-solidus conditions[29,31] from >850 °C to ~700 °C. Cooling to 600–650 °C[31] occurred ~0.5 Myr later, as shown by our titanite U–Pb age, whereas cooling to ~550 °C and below was constrained by hornblende $^{40}Ar/^{39}Ar$ dating between ~95.5 Ma and ~92 Ma[28]. The onset of cooling in the sole thus coincided with the formation of SSZ oceanic crust (96.12–95.50 Ma[25,26]). In the Semail Ophiolite, sole formation, or lower plate burial, started >8 Myr before upper plate extension occurred. The inference that underthrusting below the mantle section predated formation of the ophiolitic crust by at least 8 Myr confirms a SSZ origin for the Semail ophiolitic crust, settling the long discussion regarding its origin[29,38,39,41,50].

The Semail Ophiolite, preserving a ~50-km-wide forearc lithosphere[8] measured perpendicular to its spreading direction[38], is 8 Myr younger than the sole age, and thus does not preserve the crust of the pre-subduction initiation lithosphere. Therefore, we cannot conclude with certainty that this is the oldest SSZ crust that formed after subduction initiation. However, during SSZ spreading, the ridge must have moved away from the trench at half-spreading rate[9], which was >10 cm yr^{-1} (ref. [25]). At these rates, if upper plate spreading had started even 1 million years earlier, the ophiolite should have been ~50–100 km wider than today to preserve the 96–95.5-Myr-old crust. We therefore conclude that the oldest crust of the Semail Ophiolite formed at the onset of upper plate extension.

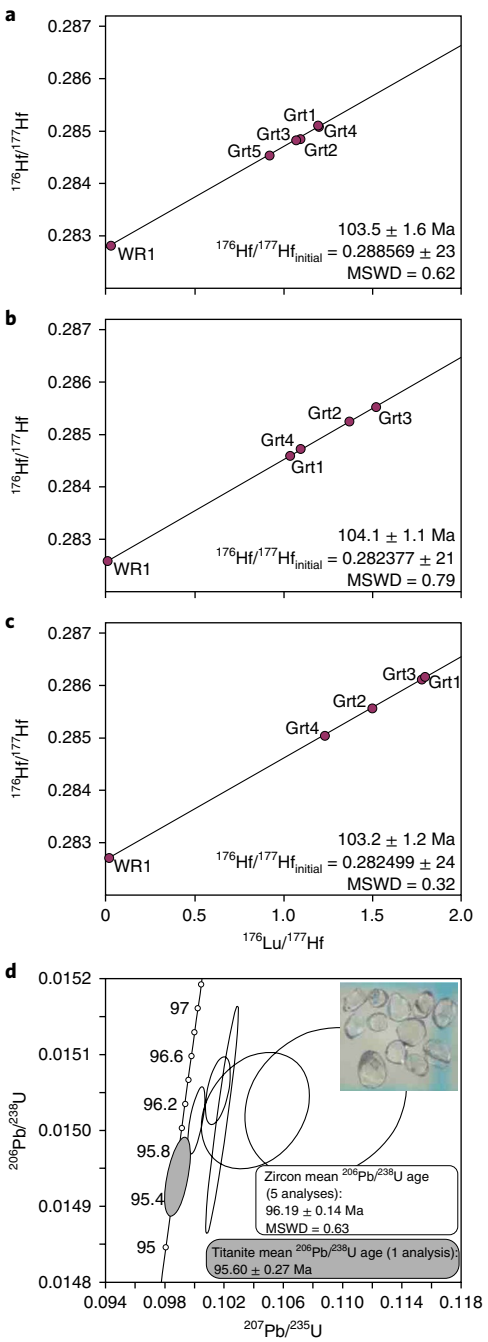

Fig. 5 | Geochronological results. a–c, Isochrons for garnet (Grt1–5) and whole rock (WR1) fractions of samples SU-03A (**a**), WT-150 (**b**) and WT-151 (**c**). Data are available in Supplementary Table 3. **d**, Concordia diagram for zircon and titanite of sample WT-151. Data point error elipses are 2σ. Inset, magnified image of zircon grains (1×1 mm). Data are available in Supplementary Table 4.

Garnet growth in the metamorphic sole at 104 Ma and the onset of SSZ crustal accretion by 96 Ma constrains a >8 Myr time lag between initial lower plate burial and the onset of upper plate extension, implying a >8 Myr period of forced convergence before upper plate extension. This time lag constitutes the first direct evidence from the geological record for ISI. The far-field causes driving the forced convergence should be sought considering the pre-104 Ma plate configuration and evolution, not the 96 Ma syn-upper plate extension configuration.

Our new results imply that SSZ ophiolite formation is not unequivocal evidence for SSI, as is often assumed for Semail and other large and well-preserved ophiolites[3,8,42]. In fact, SSZ ophiolite formation indicates the onset of upper plate extension, which does not date subduction initiation in ISI.

Both the magnitude of the time lag between initial lower plate burial and incipient upper plate extension, and the age of the onset of convergence convey critical, previously unavailable information on subduction initiation. The magnitude of the time lag should reflect the balance between forces driving and resisting upper plate extension, depending on the nature, geometry and kinematics of the intervening plates, as indicated by numerical models[2,4–6]. Longer time lags could indicate a strong upper plate, long subduction interface or slow convergence rate. Models of ISI at transform faults involving a very young upper plate[4–6] predict time lags of the order of 5–10 Myr, corresponding very well to our results. Nonetheless, the tectonic setting that led to the initiation of subduction and formation of the Semail Ophiolite must be validated from the rock record in the pre-104 Ma configuration. Accordingly, the absolute timing of initial lower plate burial is also of utmost importance. The plate configuration and kinematics in which new subduction zones were initiated in the geological past might have significantly predated the earliest expression of upper plate spreading represented by ophiolitic or modern forearc crust. Such new insights into subduction initiation processes open new avenues for reconceptualization of the initiation and processes of global plate tectonics.

Methods

Methods, including statements of data availability and any associated accession codes and references, are available at https://doi.org/10.1038/s41561-018-0209-2.

Received: 18 January 2018; Accepted: 18 July 2018;
Published online: 27 August 2018

References

1. Lithgow-Bertelloni, C. *Encyclopedia of Marine Geosciences* (eds Harff, J., Meschede, M., Petersen, S. & Thiede, J.) 193–196 (Springer, Dordrecht, 2016).
2. Stern, R. J. & Gerya, T. Subduction initiation in nature and models: a review. *Tectonophysics* https://doi.org/10.1016/j.tecto.2017.10.014 (2017).
3. Stern, R. J. Subduction initiation: spontaneous and induced. *Earth Planet. Sci. Lett.* **226**, 275–292 (2004).
4. Gurnis, M., Hall, C. & Lavier, L. Evolving force balance during incipient subduction. *Geochem. Geophys. Geosyst.* **5**, Q07001 (2004).
5. Hall, C. E., Gurnis, M., Sdrolias, M., Lavier, L. L. & Mueller, R. D. Catastrophic initiation of subduction following forced convergence across fracture zones. *Earth Planet. Sci. Lett.* **212**, 15–30 (2003).
6. Leng, W., Gurnis, M. & Asimow, P. From basalts to boninites: the geodynamics of volcanic expression during induced subduction initiation. *Lithosphere* **4**, 511–523 (2012).
7. Stern, R. J. & Bloomer, S. H. Subduction zone infancy: examples from the Eocene Izu–Bonin–Mariana and Jurassic California arcs. *Geol. Soc. Am. Bull.* **104**, 1621–1636 (1992).
8. Stern, R. J., Reagan, M., Ishizuka, O., Ohara, Y. & Whattam, S. To understand subduction initiation, study forearc crust: to understand forearc crust, study ophiolites. *Lithosphere* **4**, 469–483 (2012).
9. Van Hinsbergen, D. J. et al. Dynamics of intraoceanic subduction initiation: 2. Suprasubduction zone ophiolite formation and metamorphic sole exhumation in context of absolute plate motions. *Geochem. Geophys. Geosyst.* **16**, 1771–1785 (2015).
10. Reagan, M. K. et al. Subduction initiation and ophiolite crust: new insights from IODP drilling. *Int. Geol. Rev.* **59**, 1439–1450 (2017).
11. Arculus, R. J. et al. A record of spontaneous subduction initiation in the Izu–Bonin–Mariana Arc. *Nat. Geosci.* **8**, 728–733 (2015).
12. Faccenna, C., Becker, T. W., Lallemand, S. & Steinberger, B. On the role of slab pull in the Cenozoic motion of the Pacific plate. *Geophys. Res. Lett.* **39**, L03305 (2012).
13. Pearce, J. A., Lippard, S. J. & Roberts, S. Characteristics and tectonic significance of supra-subduction zone ophiolites. *Geol. Soc. Spec. Publ.* **16**, 74–94 (1984).
14. Dilek, Y. & Furnes, H. Ophiolite genesis and global tectonics: geochemical and tectonic fingerprinting of ancient oceanic lithosphere. *Geol. Soc. Am. Bull.* **123**, 387–411 (2011).

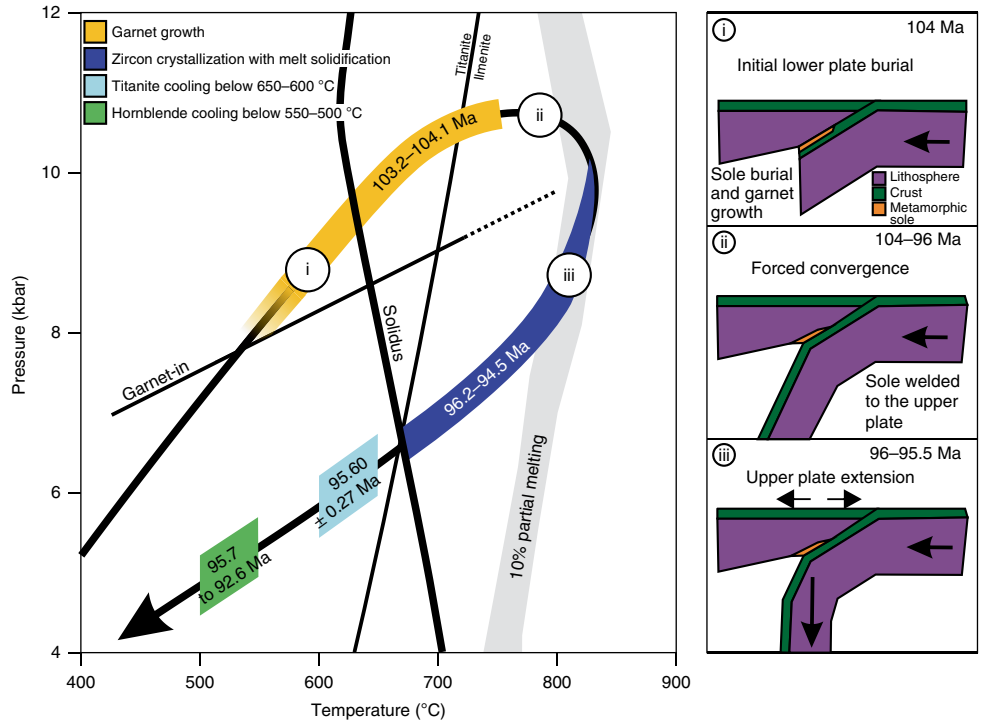

Fig. 6 | Pressure–temperature–time evolution of the Semail metamorphic sole. The pressure–temperature trajectory and hornblende ages are from Soret et al.[21]. The supra-solidus garnet growth ages and titanite ages are from this study. The zircon ages are from this study and Rioux et al.[29]. The 10% partial melting isomodes and solidus for MORB-like protoliths are from Palin et al.[23]. The garnet-in boundary and titanite–ilmenite transition are from Liu et al.[48]. i–iii, lithospheric section diagrams synthesizing our results. In iii, the spreading ages are from Rioux et al.[25,26]. See main text for details.

15. Dewey, J. F. Ophiolite obduction. *Tectonophysics* **31**, 93–120 (1976).
16. Jamieson, R. A. *P–T* paths from high temperature shear zones beneath ophiolites. *J. Metamorph. Geol.* **4**, 3–22 (1986).
17. Spray, J. G. Possible causes and consequences of upper mantle decoupling and ophiolite displacement. *Geol. Soc. Lond. Spec. Publ.* **13**, 255–268 (1984).
18. Wakabayashi, J. & Dilek, Y. Spatial and temporal relationships between ophiolites and their metamorphic soles: a test of models of forearc ophiolite genesis. *Geol. Soc. Am. Spec. Pap.* **349**, 53–64 (2000).
19. Williams, H. & Smyth, W. R. Metamorphic aureoles beneath ophiolite suites and alpine peridotites: tectonic implications with west Newfoundland examples. *Am. J. Sci.* **273**, 594–621 (1973).
20. Agard, P. et al. Plate interface rheological switches during subduction infancy: control on slab penetration and metamorphic sole formation. *Earth Planet. Sci. Lett.* **451**, 208–220 (2016).
21. Soret, M., Agard, P., Dubacq, B., Plunder, A. & Yamato, P. Petrological evidence for stepwise accretion of metamorphic soles during subduction infancy (Semail Ophiolite, Oman and UAE). *J. Metamorph. Geol.* **35**, 1051–1080 (2017).
22. Pattison, D. R. M. Petrogenetic significance of orthopyroxene-free garnet + clinopyroxene + plagioclase ± quartz-bearing metabasites with respect to the amphibolite and granulite facies. *J. Metamorph. Geol.* **21**, 21–34 (2003).
23. Palin, R. M. et al. High-grade metamorphism and partial melting of basic and intermediate rocks. *J. Metamorph. Geol.* **34**, 871–892 (2016).
24. Peacock, S. M., Rushmer, T. & Thompson, A. B. Partial melting of subducting oceanic crust. *Earth Planet. Sci. Lett.* **121**, 227–244 (1994).
25. Rioux, M. et al. Rapid crustal accretion and magma assimilation in the Oman-U.A.E. ophiolite: High precision U–Pb zircon geochronology of the gabbroic crust. *J. Geophys. Res. Solid Earth* **117**, B07201 (2012).
26. Rioux, M. et al. Tectonic development of the Samail Ophiolite: high-precision U–Pb zircon geochronology and Sm–Nd isotopic constraints on crustal growth and emplacement. *J. Geophys. Res. Solid Earth* **118**, 2085–2101 (2013).
27. Hacker, B. R. Rapid emplacement of young oceanic lithosphere: argon geochronology of the Oman Ophiolite. *Science* **265**, 1563–1565 (1994).
28. Hacker, B. R., Mosenfelder, J. L. & Gnos, E. Rapid emplacement of the Oman Ophiolite: thermal and geochronologic constraints. *Tectonics* **15**, 1230–1247 (1996).
29. Rioux, M. et al. Synchronous formation of the metamorphic sole and igneous crust of the Semail Ophiolite: new constraints on the tectonic evolution during ophiolite formation from high-precision U–Pb zircon geochronology. *Earth Planet. Sci. Lett.* **451**, 185–195 (2016).
30. Warren, C. J., Parrish, R. R., Waters, D. J. & Searle, M. P. Dating the geologic history of Oman's Semail Ophiolite: insights from U/Pb geochronology. *Contrib. Mineral. Petrol.* **150**, 403–422 (2005).
31. Yakymchuk, C., Clark, C. & White, R. W. Phase relations, reaction sequences and petrochronology. *Rev. Mineral. Geochem.* **83**, 13–53 (2017).
32. Baxter, E. F. & Scherer, E. E. Garnet geochronology: timekeeper of tectonometamorphic processes. *Elements* **9**, 433–438 (2013).
33. Scherer, E. E., Cameron, K. L. & Blichert-Toft, J. Lu–Hf garnet geochronology: closure temperature relative to the Sm–Nd system and the effects of trace mineral inclusions. *Geochim. Cosmochim. Acta* **64**, 3413–3432 (2000).
34. Smit, M. A., Scherer, E. E. & Mezger, K. Lu–Hf and Sm–Nd garnet geochronology: chronometric closure and implications for dating petrological processes. *Earth Planet. Sci. Lett.* **381**, 222–233 (2013).
35. Anczkiewicz, R. et al. Lu–Hf geochronology and trace element distribution in garnet: implications for uplift and exhumation of ultra-high pressure granulites in the Sudetes, SW Poland. *Lithos* **95**, 363–380 (2007).
36. Hacker, B. R. & Gnos, E. The conundrum of Samail: explaining the metamorphic history. *Tectonophysics* **279**, 215–226 (1997).
37. Searle, M. P., Warren, C. J., Waters, D. J. & Parrish, R. R. Structural evolution, metamorphism and restoration of the Arabian continental margin, Saih Hatat region, Oman Mountains. *J. Struct. Geol.* **26**, 451–473 (2004).
38. Nicolas, A., Boudier, F., Ildefonse, B. & Ball, E. Accretion of Oman and United Arab Emirates ophiolite—discussion of a new structural map. *Mar. Geophys. Res.* **21**, 147–180 (2000).
39. Boudier, F., Ceuleneer, G. & Nicolas, A. Shear zones, thrusts and related magmatism in the Oman Ophiolite: initiation of thrusting on an oceanic ridge. *Tectonophysics* **151**, 275–296 (1988).
40. Ishikawa, T., Nagaishi, K. & Umino, S. Boninitic volcanism in the Oman Ophiolite: implications for thermal condition during transition from spreading ridge to arc. *Geology* **30**, 899–902 (2002).
41. MacLeod, C. J., Lissenberg, L. & Bibby, L. E. "Moist MORB" axial magmatism in the Oman Ophiolite: the evidence against a mid-ocean ridge origin. *Geology* **41**, 459–462 (2013).
42. Whattam, S. A. & Stern, R. J. The "subduction initiation rule": a key for linking ophiolites, intra-oceanic fore-arcs, and subduction initiation. *Contrib. Mineral. Petrol.* **162**, 1031–1045 (2011).
43. Agard, P., Jolivet, L., Vrielynck, B., Burov, E. & Monié, P. Plate acceleration: the obduction trigger? *Earth Planet. Sci. Lett.* **258**, 428–441 (2007).

44. Duretz, T. et al. Thermo-mechanical modeling of the obduction process based on the Oman Ophiolite case. *Gondwana Res.* **32**, 1–10 (2016).
45. Cowan, R. J., Searle, M. P. & Waters, D. J. Structure of the metamorphic sole to the Oman Ophiolite, Sumeini Window and Wadi Tayyin: implications for ophiolite obduction processes. *Geol. Soc. Lond. Spec. Publ.* **392**, 155–175 (2014).
46. Gnos, E. Peak metamorphic conditions of garnet amphibolites beneath the Semail Ophiolite: implications for an inverted pressure gradient. *Int. Geol. Rev.* **40**, 281–304 (1998).
47. Rioux, M., Bowring, S., Cheadle, M. & John, B. Evidence for initial excess ^{231}Pa in mid-ocean ridge zircons. *Chem. Geol.* **397**, 143–156 (2015).
48. Liu, J., Bohlen, S. R. & Ernst, W. G. Stability of hydrous phases in subducting oceanic crust. *Earth Planet. Sci. Lett.* **143**, 161–171 (1996).
49. Bloch, E., Ganguly, J., Hervig, R. & Cheng, W. ^{176}Lu–^{176}Hf geochronology of garnet I: experimental determination of the diffusion kinetics of Lu^{3+} and Hf^{4+} in garnet, closure temperatures and geochronological implications. *Contrib. Mineral. Petrol.* **169**, 12 (2015).
50. Ishikawa, T., Fujisawa, S., Nagaishi, K. & Fujisawa, T. Trace element characteristics of the fluid liberated from amphibolite-facies slab: inference from the metamorphic sole beneath the Oman Ophiolite and implication for boninite genesis. *Earth Planet. Sci. Lett.* **240**, 355–377 (2005).
51. Sun, S.-s. & McDonough, W. F. Chemical and isotopic systematics of oceanic basalts: implications for mantle compositions and processes. *Geol. Soc. Spec. Publ.* **42**, 313–345 (1989).

Acknowledgements

This research was financially supported by the Natural Sciences and Engineering Research Council of Canada (Discovery Grant RGPIN-2014-05681 to C.G. and RGPIN-2015-04080 to M.A.S.), the Canadian Foundation for Innovation (Projects 34991 to C.G. and 229814 to M.A.S.) and European Research Council (Starting Grant 306810 (SINK) and NWO Vidi grant 864.11.004 to D.J.J.v.H). We thank M. Al Battashi (Sultanate of the Oman Ministry of Commerce and Industry, Directorate General of Minerals) for permission to undertake field sampling in Oman.

Author contributions

C.G. generated the project, led the field work, completed the petrological study and wrote the manuscript. M.S. conducted the Lu–Hf analyses and contributed to writing the manuscript. D.J.J.v.H. participated in the field work, and contributed to the rationale and writing of the manuscript. D.G. and F.C. completed the U–Pb geochronological analyses. B.C. planned and participated in the field work, and prepared and analysed the samples. M.M. organized and participated in the field work. O.R. participated in defining the rationale and writing the manuscript. D.S. conducted the laser ablation ICP analyses.

Competing interests

The authors declare no competing interests.

Additional information

Supplementary information is available for this paper at https://doi.org/10.1038/s41561-018-0209-2.

Correspondence and requests for materials should be addressed to C.G.

Methods

Representative thin sections for each sample were mapped using a Bruker M4 TORNADO micro-X-ray fluorescence instrument at Université Laval (Fig. 3a–c) equipped with two 60 mm^2 Silicon Drift Detectors, operating at 50 kv and 300 nA with a step size of 20 µm and a dwell time of 3 ms pixel^{-1}, to find garnet grain sections that intersected the core. These garnet grains were subjected to major-element quantitative point analysis along radial profiles using a Cameca SX-100 five sprectrometer electron probe microanalyser at Université Laval. Analytical conditions were 15 kV and 20 nA, with a counting time of 20 s on peaks and 10 s on background. The calibration standards used were generally simple oxides (GEO Standard Block; P&H Developments), or minerals where needed (Mineral Standard Mount MINM25-53; Astimex Scientific; reference samples from ref. [52]). Data were reduced using the PAP model[53]. The data are available in Supplementary Table 1 and Fig. 3h–j.

Trace element analysis of the garnet sections was done by laser ablation inductively coupled plasma mass spectrometry (ICP-MS) at LabMaTer (Université du Québec à Chicoutimi), using a RESOlution 193 nm excimer laser (Australian Scientific Instruments) and an S155 Laurin Technic ablation cell system coupled to an Agilent 7900 quadrupole ICP-MS. Spot analyses were conducted with a 33 µm beam operating at 15 Hz and 5 J cm^{-2} in a 4 ms isotope^{-1} cycle. High-resolution mapping was done with a 20 µm beam at a speed of 80 µm s^{-1} (Fig. 4a,c,e) and pulsing of 30 Hz at 5 J cm^{-2} in a 4 ms isotope^{-1} cycle. The calibrant used was the synthetic basalt glass GSE-1G (USGS), using preferred values from the Geological and Environmental Reference Materials (GeoReM) database[54]. The data were processed with Iolite freeware[55] to generate maps and achieve fully quantitative results on spots analysis using ^{29}Si as an internal standard. The data are available in Supplementary Table 2 and Fig. 4.

For garnet Lu–Hf and zircon U–Pb geochronology, samples were disaggregated using an Electric Pulse Disaggregation instrument at Overburden Drilling Management to 90% < 1 mm. Bulk-rock powders were created from this fraction. Large garnet concentrates of 800 mg or more were extracted from the samples through standard concentration methods: sieving, magnetic separation using a Frantz magnetic barrier separator, heavy liquor density separation and handpicking on a binocular microscope. Zircon and titanite grains were handpicked from the heavy mineral fraction.

Garnet Lu–Hf chronology was done at the Pacific Centre for Isotopic and Geochemical Research, University of British Columbia. There, garnet crystals and bulk-rock powder were transferred to screw-top perfluoroalkoxy alkanes (PFA) vials and weighed. Garnet grains were then washed using deionized water and bathed in 1 N HCl at room temperature for 1 h. After removing the HCl, garnet samples were dried, mixed with a ^{176}Lu–^{180}Hf isotope tracer with a Lu/Hf value similar to that of generic garnet, and digested through the repeated addition of HF:HNO_3:$HClO_4$ and 6 N HCl, each step followed by evaporation to dryness. After admixing of a mixed ^{176}Lu–^{180}Hf isotope tracer with a low Lu/Hf value, the bulk-rock powders were digested in a stainless-steel digestion vessel at 180 °C for 7 days using HF:HNO_3.

After digestion, all samples were dried down, re-dissolved in 6 N HCl, diluted to 3 N HCl using deionized water and centrifuged. The solution containing the garnet elemental solute was then loaded onto polypropylene columns containing a 1 ml Ln-spec resin bed and subjected to rare earth elements and high field-strength elements chromatography modified from the method of Münker et al.[56]. Isotope analyses for hafnium and lutetium were done using the Nu Instruments *Plasma HR* multi-collector ICP-MS at the Pacific Centre for Isotopic and Geochemical Research. For lutetium analyses, isobaric interference of ^{176}Yb on *m/z* corresponding to a mass of 176 was corrected using an exponential correlation between ^{176}Yb/^{171}Yb and ^{174}Yb/^{171}Yb. This correlation was calibrated through replicate analyses of ytterbium solution standards from the National Institute of Standards and Technology performed at different concentrations (10–100 ppb[57]). For hafnium isotope analyses, ^{180}Ta and ^{180}W interferences were estimated on the basis of ^{181}Ta/^{177}Hf and ^{183}W/^{177}Hf, assuming natural abundance and a hafnium-based mass bias. Mass bias was assumed to follow an exponential law and was corrected for by applying ^{179}Hf/^{177}Hf = 0.7325 (hafnium, tantalum and tungsten) and ^{173}Yb/^{171}Yb = 1.1296 (lutetium and ytterbium). Any resolvable drift was corrected for assuming linear time dependence. Hafnium isotope ratios are reported relative to the JMC-475 hafnium standard (^{176}Hf/^{177}Hf = 0.28216; ref. [58]). The external ^{176}Hf/^{177}Hf reproducibility (2 s.d.) of replicate JMC-475 analyses performed at concentrations similar to those of sample solutions was 0.4 ε_{Hf} during the course of our analytical sessions. The external reproducibility of ^{176}Hf/^{177}Hf was estimated from the standard scatter at the given sample concentration and internal error. This estimate was made by comparing internal and external uncertainty for replicate analyses of JMC-475 performed at concentrations that bracketed those of the samples (10–50 ppb[59]). The Lu–Hf isochrons were established using Isoplot version 3.27 (ref. [60]), applying 1.876×10^{-11} yr^{-1} for λ^{176}Lu[61,62]. All uncertainties are cited at the 2 s.d. level. The results are provided in Supplementary Table 3 and Fig. 5.

The samples were screened for zircon and titanite, and both minerals were found only in sample 151A. After selection under an optical microscope, zircon was subjected to chemical abrasion[63,64], whereas titanite was not abraded. The selected grains were then spiked with a ^{202}Pb–^{205}Pb–^{235}U tracer, followed by dissolution, chemical separation of lead and uranium, and mass spectrometry, after the procedure detailed in Krogh[65] with modifications described in Corfu[66]. The lead measurements were performed mostly with an ion-counting secondary electron multiplier. The obtained data were corrected with fractionation factors determined from the 205Pb/202Pb ratio of the tracer (around 0.1% amu^{-1} for lead) and 0.12% amu^{-1} for uranium, subtracting blanks of 0.1 pg uranium and 2 pg lead, or less when the total common lead was below that level. The remaining initial lead was corrected using compositions calculated with the model of Stacey and Kramers[67]. The data were also adjusted for a deficit of ^{206}Pb due to initial deficiency of ^{230}Th (ref. [68]) and the tracer was calibrated with reference to the ET100 solution. Plotting and regressions were done with the Isoplot software package[60]. The decay constants are those of Jaffey et al.[69]. The results are provided in Supplementary Table 4 and Fig. 5.

Data availability. The authors declare that all the data supporting the findings of this study are available within the paper and its Supplementary Information files.

References

52. Jarosewich, E., Nelen, J. A. & Norberg, J. A. Reference samples for electronmicroprobe analysis. *Geostand. Newslett.* **4**, 43–47 (1980).
53. Pouchou, J.-L. & Pichoir, F. in *Electron Probe Quantification* (eds Heinrich, K. & Newbury, D.) 31 75 (Springer, New York, 1991).
54. Jochum, K. P. et al. GeoReM: a new geochemical database for reference materials and isotopic standards. *Geostand. Geoanal. Res.* **29**, 333–338 (2005).
55. Paton, C., Hellstrom, J., Paul, B., Woodhead, J. & Hergt, J. Iolite: freeware for the visualisation and processing of mass spectrometric data. *J. Anal. Atom. Spectrom.* **26**, 2508–2518 (2011).
56. Münker, C., Weyer, S., Scherer, E. E. & Mezger, K. Separation of high field strength elements (Nb, Ta, Zr, Hf) and Lu from rock samples for MS-ICPMS measurements. *Geochem. Geophys. Geosyst.* **2**, 2001GC000183 (2001).
57. Blichert-Toft, J., Boyet, M., Télouk, P. & Albarède, F. ^{147}Sm–^{143}Nd and ^{176}Lu–^{176}Hf in eucrites and the differentiation of the HED parent body. *Earth Planet. Sci. Lett.* **204**, 167–181 (2002).
58. Blichert-Toft, J., Chauvel, C. & Albarede, F. Separation of Hf and Lu for high precision isotope analysis of rock samples by magnetic sector-multiple collector ICP-MS. *Contrib. Mineral. Petrol.* **127**, 248–260 (1997).
59. Bizzarro, M., Baker, J. A. & Ulfbeck, D. A new digestion and chemical separation technique for rapid and highly reproducible determination of Lu/Hf and Hf isotope ratios in geological materials by MC-ICP-MS. *Geostand. Geoanal. Res.* **27**, 133–145 (2003).
60. Ludwig, K. R. *Isoplot 4.1. A Geochronological Toolkit for Microsoft Excel* (Berkeley Geochronology Center, 2009).
61. Scherer, E. E., Mezger, K. & Münker, C. The ^{176}Lu decay constant discrepancy: terrestrial samples vs. meteorites. *Meteorit. Planet. Sci.* **38**, A136 (2003).
62. Söderlund, U., Patchett, P. J., Vervoort, J. D. & Isachsen, C. E. The ^{176}Lu decay constant determined by Lu–Hf and U–Pb isotope systematics of Precambrian mafic intrusions. *Earth Planet. Sci. Lett.* **219**, 311–324 (2004).
63. Mattinson, J. M. Zircon U–Pb chemical abrasion ("CA-TIMS") method: combined annealing and multi-step partial dissolution analysis for improved precision and accuracy of zircon ages. *Chem. Geol.* **220**, 47–66 (2005).
64. Mattinson, J. M. Analysis of the relative decay constants of ^{235}U and ^{238}U by multi-step CA-TIMS measurements of closed-system natural zircon samples. *Chem. Geol.* **275**, 186–198 (2010).
65. Krogh, T. E. A low-contamination method for hydrothermal decomposition of zircon and extraction of U and Pb for isotopic age determinations. *Geochim. Cosmochim. Acta* **37**, 485–494 (1973).
66. Corfu, F. U–Pb age, setting and tectonic significance of the anorthosite–mangerite–charnockite–granite suite, Lofoten–Vesterålen, Norway. *J. Petrol.* **45**, 1799–1819 (2004).
67. Stacey, J. S. & Kramers, J. D. Approximation of terrestrial lead isotope evolution by a two-stage model. *Earth Planet. Sci. Lett.* **26**, 207–221 (1975).
68. Schärer, U. The effect of initial ^{230}Th disequilibrium on young U–Pb ages: the Makalu case, Himalaya. *Earth Planet. Sci. Lett.* **67**, 191–204 (1984).
69. Jaffey, A. H., Flynn, K. F., Glendenin, L. E., Bentley, W. C. & Essling, A. M. Precision measurement of half-lives and specific activities of ^{235}U and ^{238}U. *Phys. Rev. C* **4**, 1889–1906 (1971).